Acta Pharmaceutica Sinica B 2025;15(6):2884−2899

Chinese Pharmaceutical Association
Institute of Materia Medica, Chinese Academy of Medical Sciences

Acta Pharmaceutica Sinica B

www.elsevier.com/locate/apsb
www.sciencedirect.com

ORIGINAL ARTICLE

Nose-to-brain delivery of targeted lipid nanoparticles as two-pronged β-amyloid nanoscavenger for Alzheimer's disease therapy

Yanyan Xu[a,b], Xiangtong Ye[b], Yanfeng Du[a], Wenqin Yang[b], Fan Tong[b], Wei Li[a], Qianqian Huang[b], Yongke Chen[b], Hanmei Li[c], Huile Gao[b,*], Weiwei Zhang[a,*]

[a]*School of Public Health, Chengdu Medical College, Chengdu 610500, China*
[b]*Key Laboratory of Drug-Targeting and Drug Delivery System of the Education Ministry and Sichuan Province, Sichuan Engineering Laboratory for Plant-Sourced Drug and Sichuan, Research Center for Drug Precision Industrial Technology, West China School of Pharmacy, Sichuan University, Chengdu 610041, China*
[c]*School of Food and Biological Engineering, Chengdu University, Chengdu 610106, China*

Received 14 January 2025; received in revised form 24 February 2025; accepted 26 February 2025

KEY WORDS

Nose-to-brain delivery;
Lipid nanoparticle;
Alzheimer's disease;
β-Amyloid clearance;
α-Mangostin;
β-Site APP cleaving enzyme 1;
Targeted delivery;
Synergistic therapy

Abstract Alzheimer's disease (AD), characterized by β-amyloid (Aβ) aggregation and neuroinflammation, remains a formidable clinical challenge. Herein, we present an innovative nose-to-brain delivery platform utilizing lactoferrin (Lf)-functionalized lipid nanoparticles (LNPs) co-encapsulating α-mangostin (α-M) and β-site APP cleaving enzyme 1 (BACE1) siRNA (siB). This dual-modal therapeutic system synergistically combines the neuroprotective and microglia-reprogramming capabilities of α-M with the transcriptional silencing of BACE1 *via* siB, thereby simultaneously inhibiting Aβ production and enhancing its clearance. Fabricated *via* a microfluidic approach, the LNPs exhibited uniform particle size distribution, great encapsulation efficiency, and robust colloidal stability. Upon intranasal administration, Lf-functionalization enabled superior brain-targeting efficacy through receptor-mediated transcytosis. *In vitro* studies demonstrated that α-M reversed Aβ-induced low-density lipoprotein receptor downregulation, promoting microglial phagocytosis and autophagic degradation of Aβ, while siB effectively suppressed BACE1 expression, abrogating Aβ synthesis. *In vivo* investigations in APP/PS1 transgenic mice revealed remarkable cognitive recovery, substantial Aβ plaque reduction, and alleviation of neuroinflammation and oxidative stress. This intricately designed LNP system, exploiting a non-invasive and efficient nose-to-brain delivery route, provides a biocompatible, synergistic, and transformative therapeutic strategy for the multifaceted management of AD.

---

*Corresponding authors.
E-mail addresses: gaohuile@scu.edu.cn (Huile Gao), solozww@163.com (Weiwei Zhang).

Peer review under the responsibility of Chinese Pharmaceutical Association and Institute of Materia Medica, Chinese Academy of Medical Sciences.

https://doi.org/10.1016/j.apsb.2025.02.035

1. Introduction

Fueled by the extended life expectancy, AD has emerged as a major public health concern with a sharp rise in its global prevalence, contributing to significant medical and financial burdens[1-3]. Constrained by modest symptomatic relief and a narrow target population, current clinical AD treatments are of limited benefit[4,5]. In AD pathogenesis, accumulated Aβ plaque is a leading hallmark, which induces inflammation and triggers neuronal toxicity[6-8]. Recent approvals of Aducanumab and Lecanemab manifested the feasibility of Aβ-associated macromolecular therapeutics, on account of superior target precision, disease-modifying potential, and less off-target effect[6,9-11]. However, both the unsatisfactory clinical outcomes and non-negligible adverse events underscored the imperative demands for more effective and safer AD remedies[9,12,13].

Compared to the aforementioned monoclonal antibodies, nucleic acid-based genetic drugs, such as siRNA, can directly reprogram the central dogma of biology to prevent and treat diseases[14]. For instance, the first approved siRNA drug, Onpattro (patisiran), targets and degrades the messenger RNA of transthyretin, mitigating the production of misfolded proteins in hereditary transthyretin-mediated amyloidosis[15,16]. Similarly, β-site APP cleaving enzyme 1 (BACE1) plays a crucial role in the formation of Aβ plaques, which can be silenced *via* BACE1 siRNA (siB), thus obstructing the onset of subsequent cascades such as neuroinflammation and neurodegeneration in the early phase of AD[17-20]. In addition, for AD patients suffering from the advanced stage, it is also indispensable to clear existing Aβ plaques and modulate the inflammatory brain microenvironment[21,22]. α-Mangostin (α-M) is a natural polyphenolic compound, exhibiting a potent antioxidant activity to alleviate oxidative stress and shield neurons from further damage. Besides the anti-inflammatory effect, α-M also possesses the capability to upregulate low-density lipoprotein receptor (LDLR) expression in microglia to facilitate Aβ uptake and reprogram metabolism in the disease-associated microglial to holistically rejuvenate Aβ clearance capacity[23,24]. Therefore, the combination of siB and α-M is anticipated to be a thorough AD regimen that encompasses the full spectrum of AD stages. Nevertheless, siRNA is a negatively charged macromolecule, and α-M is lipophilic, both of which are highly susceptible to degradation when exposed to the bloodstream. Therefore, the urge for optimized drug delivery platforms is elemental, thus realizing better stability, greater biodistribution to the desired site of action, and implementing the full potential of this combination therapy.

Following the prominent success garnered by COVID-19 mRNA vaccines, ionizable cationic LNP has emerged in the limelight for nucleic acid therapeutic delivery[25,26]. LNP is the most clinically state-of-the-art non-viral gene delivery platform, featuring outstanding delivering potency, biocompatibility, and the capability for repeated administration, which favors clinical translation[27,28]. At the same time, due to the lipid vesicle structure, LNP is also eligible for encapsulating liposoluble small-molecular therapeutics such as α-M, thereby becoming an optimal selection to load and deliver siB and α-M simultaneously. However, upon intravenous injection, the adsorption of proteins in the blood and the formation of protein corona leads to the liver tropism of LNP[29-32]. Consequently, intranasal administration surpasses conventional intravenous routes by offering a non-invasive, efficient, and direct pathway to the brain, circumventing the BBB and ensuring enhanced patient compliance[19,33-36]. Drugs administered intranasally can traverse the trigeminal and olfactory nerve pathways, utilizing axonal transport to further extend to the olfactory bulb and brain stem, guaranteeing high bioavailability, expeditious onset of action, improved patient compliance, and reduced systemic toxicity[34,37-39]. To prolong residence time and carry out higher brain entry efficiency, it is of great necessity to tailor specific targeting moiety on the surface of LNP, which is viable due to the manifold functional groups offered by lipids[28,40-42]. Given that the lactoferrin (Lf) receptor is upregulated in both respiratory epithelial cells and neurons for AD patients, Lf is exploited to embellish LNP to accomplish dual targeting[43-46]. Overall, engineering an LNP modified by Lf to simultaneously deliver α-M and siB (α-M/siB@L-Lf) *via* a nose-to-brain route represents a groundbreaking paradigm of AD therapy. More significantly, supplementing with mucolytic agents such as *N*-acetyl cysteine (NAC) was critical for improving the permeation by dissolving mucus and enhancing the targeting efficiency of nose-to-brain delivery[37,41].

Herein, the nose-to-brain targeted α-M/siB@L-Lf was contrived and co-administered with NAC (α-M/siB@L-Lf + N) to scavenge Aβ in a two-pronged manner for AD treatment (Scheme 1). Following intranasal administration, Lf-conjugated LNPs were delivered to the brain and then neurons *via* clathrin-mediated endocytosis[44-47]. Upon release from the nanoparticles, α-M and siB synergistically target Aβ pathology through distinct yet complementary mechanisms, curtailing its generation while facilitating its elimination. *In vivo* and *in vitro* data validated the synergistic potency of α-M/siB@L-Lf, triumphantly achieving the remodeling of abnormal lesion microenvironment and the rescue of cognitive loss. Collectively, this nanosystem represented a significant advancement, merging an innovative delivery route with a synergistic therapeutics strategy to address the multifaceted pathology of AD.

2. Materials and methods

2.1. Materials

SM-102, DSPC, and DMG-PEG$_{2000}$ were obtained from AVT Pharmaceutical Tech Co., Ltd. (Shanghai, China). Cholesterol and NAC was purchased from Macklin Biochemical Technology Co., Ltd. (Shanghai, China). DSPE-PEG$_{2000}$-Mal was purchased from Yusi Medical Technology Cable Co., Ltd. (Chongqing, China). 2-Iminothiolane hydrochloride, lactoferrin (from bovine milk), and α-mangostin were all available from Aladdin Biochemical Technology Co., Ltd. (Shanghai, China). The BACE1 siRNA (sense: GCUUUGUGGAGAUGGUGGATT, antisense: UCCACCAUC UCCACAAAGCTT), negative control siRNA (sense:

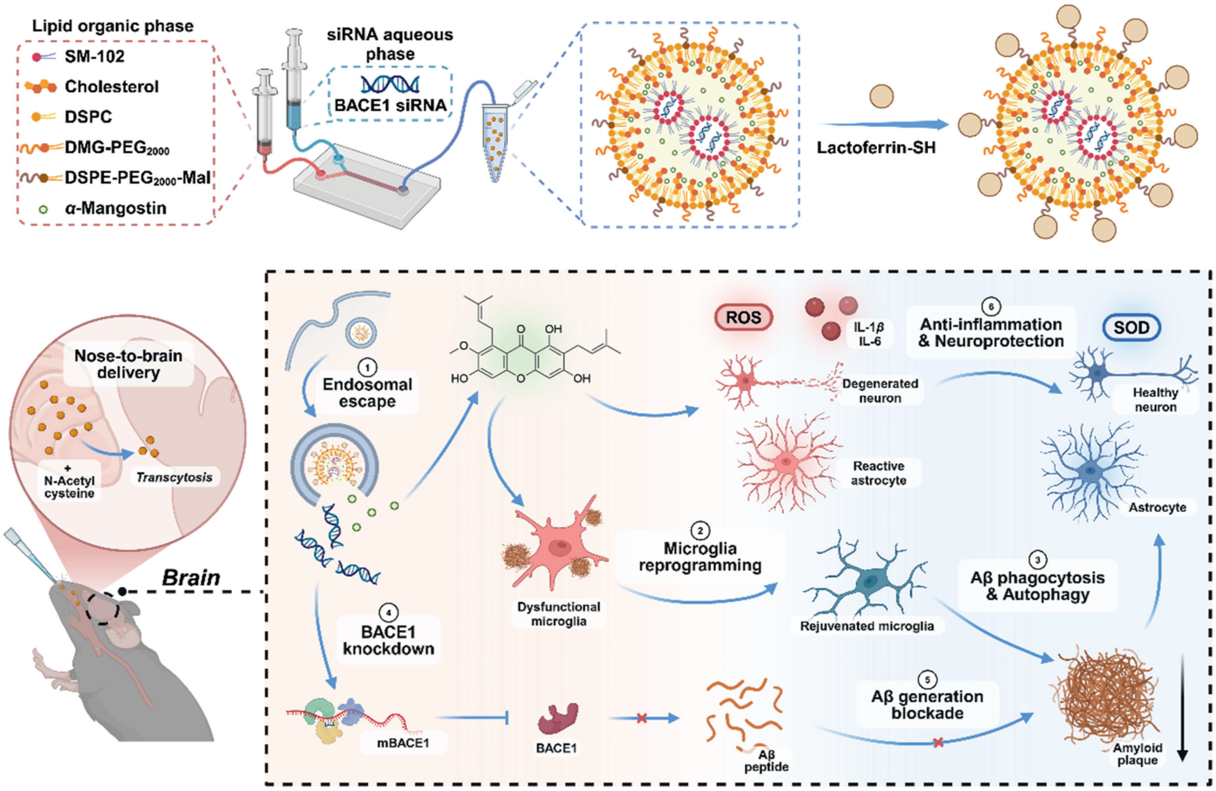

Scheme 1 The fabrication of α-M/siB@L-Lf and the mechanism of two-pronged Aβ scavenging therapy of the intranasally administered α-M/siB@L-Lf + N in AD. Created with BioRender.com.

UUCUCCGAACGUGUCACGUTT, antisense: ACGUGACACGUUCGGAGAATT), and Cy5-negative control siRNA were purchased from Genemed Biotechnology Co., Ltd. (Chengdu, China). Amyloid-β (1−42) peptide (Aβ_{1-42}) and FITC-amyloid-β (1−42) peptide (FITC-Aβ_{1-42}) were purchased from GL Biochem Ltd. (Shanghai, China). Complete Dulbecco's modified Eagle's medium (DMEM), trypsin-EDTA solutions, and fetal bovine serum (FBS) were purchased from Gibco (USA). The anti-BACE1, anti-LDLR, anti-APP, anti-GAPDH, anti-β-tubulin, anti-β-actin antibodies, and horseradish peroxidase-conjugated goat anti-rabbit and goat anti-mouse IgG (H + L) secondary antibodies were purchased from ABclonal Technology Co., Ltd. (Wuhan, China). The anti-LC3B antibody was obtained from Cell Signaling Technology, Inc. (USA). ELISA kits (BACE1 and Aβ_{1-42}) were purchased from Ruixin Biotechnology Co., Ltd. (Quanzhou, China). Enzyme-linked immunosorbent assay (ELISA) kits (IL-1β and IL-6) were purchased from BD Pharmingen (USA). All chemicals utilized were of analytical or reagent-grade quality.

2.2. *Cell lines and animals*

The BV-2, PC-12, and Calu-3 cell lines were obtained from the Chinese Academy of Sciences Cell Bank (Shanghai, China). Male C57BL/6 mice were provided by SPF Biotechnology Co., Ltd. (Beijing, China). Male APP/PS1 mice were purchased from Changzhou Cavens Experimental Animal Co., Ltd. All animals were raised under standard housing conditions. All animal experiments were performed in accordance with the guidelines laid down and approved by the experimental animal management committee of Sichuan University. The assigned approval/accreditation number was KS2020420.

2.3. *Preparation of LNPs and Lf-LNPs*

A microfluidic-chip device from Nexstar Nano Technology Co., Ltd. (Shanghai, China) was employed to fabricate the LNPs with uniform particle size. The lipid ethanol phase contained a mixture of SM-102, DSPC, cholesterol, DMG-PEG$_{2000}$, and DSPE-PEG$_{2000}$-Mal at molar ratios of 42:13:43:1.5:0.5. siR was dissolved in 20 mmol/L sodium acetate (NaOAc) buffer (pH 4.0) to compose the siRNA aqueous phase. The two phases were connected separately to the corresponding syringes, and the volume ratio of the organic phase to the aqueous phase was 1:3. The resulting LNPs were obtained through rapid mixing of the two channels of the chip at a total flow rate of 12 mL/min. The LNPs were then ultrafiltered (MW = 10 kDa) three times to remove the ethanol and replace the buffer with 1 × phosphate-buffered saline (PBS) (pH 7.2).

For Lf decoration, Lf was first thiolated in reaction with a 5:1 M excess of 2-iminothiolane hydrochloride in 0.15 mol/L sodium borate buffer (pH 8.0 supplemented with 0.1 mmol/L EDTA) under nitrogen at room temperature for 1 h. Then, the thiolated Lf was ultrafiltered (MW = 30 kDa) three times with 1 × PBS (pH 7.2) to remove excess 2-iminothiolane hydrochloride. The LNPs were mixed with previously prepared thiolated Lf and continuously reacted under nitrogen at room temperature for 12 h. The Lf-decorated LNPs were ultrafiltered (MW = 100 kDa) three times with 1 × PBS (pH 7.2) to remove excess unreacted Lf.

2.4. Agarose gel electrophoresis assay

Agarose was dissolved in tris acetate/EDTA (TAE) buffer and mixed with GelRed to form 2% agarose gel. Negative control siRNA (NC) was encapsulated in LNP (NC@L) at 1:1, 2:1, 4:1, 8:1, 12:1, and 16:1 N/P ratios, respectively. The samples were diluted in the loading buffer. The mixtures were separated *via* electrophoresis for 20 min at 100 V. The gel was detected and photographed using the UV illuminator.

2.5. Cellular uptake

PC-12 cells were seeded in 12-well plates at a density of 4×10^4 cells per well. After achieving appropriate confluency, the culture medium was removed and cells were washed with PBS (pH 7.2) twice. Cy5-labeled NC encapsulated by LNPs (Cy5-NC@L) and Lf-decorated LNPs (Cy5-NC@L-Lf) were diluted in FBS-free medium at the same concentration of Cy5-NC were added to the plates respectively and incubated for 0.5, 2, and 4 h, respectively. Subsequently, the cells were washed three times with PBS (pH 7.2), digested and dispersed in 0.4 mL PBS for flow cytometry (FCM, Agilent NovoCyte, Palo Alto, USA). For fluorescence imaging observation, PC-12 cells were planted into 12-well plates covered with a round coverslip, and the administration protocol was consistent with the flow cytometry analysis. After incubation, the coverslips were washed three times with PBS, fixed with 4% paraformaldehyde, stained with DAPI solution (2 μg/mL) for 5 min, washed again, immersed in Antifade Mounting Medium (Solarbio Life Science, Beijing), and ultimately sealed for confocal laser scanning microscope (CLSM) (Leica, DMi8, Weztlar, Germany) observation. Calu-3 cells were processed with the same protocol.

2.6. $A\beta_{1-42}$ oligomer preparation

Lyophilized human $A\beta_{1-42}$ monomer peptide, purified by HPLC (>95%), was used to generate $A\beta_{1-42}$ oligomers following a previously described protocol[48]. The $A\beta_{1-42}$ monomer was first dissolved in anhydrous DMSO to a concentration of 2 mmol/L, then diluted in ice-cold Opti-MEM to achieve a final concentration of 100 μmol/L. After vortexing for 30 s, the resulting solution was incubated at 4 °C for 24 h prior to use.

2.7. Cellular phagocytosis

BV-2 cells were seeded in 12-well plates at a density of 5×10^4 cells per well. After achieving appropriate confluency, the cells were treated with α-M/NC@L-Lf at different α-M concentrations for 24 h. At the last 3 or 1 h of the treatment, the culture medium was replaced with fresh medium containing 2 μmol/L FITC-$A\beta_{1-42}$. After incubation, the cells were washed three times with cold PBS (pH 7.2), digested, and collected to quantify the fluorescence of FITC *via* flow cytometry (Agilent). For qualitative analysis of cellular phagocytosis, cover slides with BV-2 cells were prepared. The treatment scheme was the same as the quantitative analysis. After incubation, the slices were processed with the same method as the cellular uptake protocol for CLSM (Leica) observation.

For the mechanism exploration, BV-2 cells were seeded in 6-well plates at a density of 2×10^5 cells per well. After achieving appropriate confluency, the cells were treated with α-M/NC@L-Lf at different α-M concentrations and 8 μmol/L $A\beta_{1-42}$ oligomers for 24 h. Then, the cells were washed three times with cold PBS (pH 7.2) and lysed using RIPA lysis buffer (Beyotime Biotechnology, Shanghai) to obtain the total protein. The protein was mixed with 5 × SDS-PAGE sample loading buffer (Beyotime Biotechnology, Shanghai), boiled for 10 min for full denaturation, and subjected to western blotting analysis for the detection of LDLR expression.

2.8. Autophagy activation effects in vitro

BV-2 cells were seeded in 6-well plates at a density of 2×10^5 cells per well. After achieving appropriate confluency, the cells were treated with different preparations and 8 μmol/L $A\beta_{1-42}$ oligomers for 24 h. The final concentration of α-M was 400 ng/mL. Then, the cells were harvested and processed with the method of western blotting mentioned above, thus obtaining the expression level of autophagosome marker LC3B.

2.9. Quantitative real-time PCR in vitro

The upregulation of LDLR expression and endogenous BACE1 gene silencing ability of LNPs were investigated by quantitative real-time PCR (qRT-PCR).

LDLR: BV-2 cells were seeded in a 12-well plate at a density of 5×10^4 cells per well. After achieving appropriate confluency, the cells were treated with different preparations and 8 μmol/L $A\beta_{1-42}$ oligomers for 24 h. The final concentration of α-M was 400 ng/mL. The total RNA was extracted using the Cell Total RNA Isolation Kit (Foregene, China), and then reverse transcribed into cDNA using a Hifair® III 1st Strand cDNA Synthesis SuperMix (Yeasen, China). Later, qRT-PCR was performed according to BrightCycle Universal SYBR Green qPCR Mix with UDG (ABclonal, China).

BACE1: PC-12 cells were seeded in a 12-well plate at a density of 5×10^4 cells per well. After achieving appropriate confluency, the cells were treated with different preparations and 8 μmol/L $A\beta_{1-42}$ oligomers for 24 h. The final concentration of siB was 400 nmol/L. The following qRT-PCR procedures were outlined above.

The primer and reverse primer sequences are as follows: BACE1: F, GGAACCCATCTCGGCATCC; R, TCCGATTCCT CGTCGGTCTC; LDLR: F, GAAGGCAGCTACAAGTGTGAG; R, GGGGAGCAGACTGGTGTACT; and β-actin: F, GGCTGTA TTCCCCTCCATCG; R, CCAGTTGGTAACAATGCCATGT.

2.10. Neuroprotective efficacy assessment

PC-12 cells were seeded in 96-well plates at a density of 4×10^3 cells per well and incubated for 12 h. Then, the medium was removed and the cells were treated with fresh medium containing 20 μmol/L $A\beta_{1-42}$ oligomers and various treatments (α-M 400 ng/mL, siB 400 nmol/L). After 36 h co-culture, the medium was replaced with DMEM medium, and the cell viability was assessed *via* MTT assay.

2.11. Evaluation of nasal epithelial barrier penetration

Calu-3 cells were seeded in the insert of the Transwell plate (12 wells, pore size: 0.4 μm, Corning, USA) at a density of 3×10^4 cells per well to obtain a nasal epithelial cell model. The culture medium was changed daily, and the transepithelial electrical resistance (TEER) value was detected regularly (Millicell-ERS, Millipore, USA) and calculated as Eq. (1):

$$\mathrm{TEER} = \left(R_{\mathrm{sample}} - R_{\mathrm{blank}}\right) \cdot A \tag{1}$$

where R_{sample} was the resistance in cell-seeded wells, R_{blank} was the resistance in blank wells without cells, and A was the surface area of the membrane in the insert.

When the TEER value reached about 500 $\Omega \cdot \mathrm{cm}^2$, the culture condition was converted to an air-liquid interface (ALI), allowing the differentiation of Calu-3 cells to obtain a tight epithelial barrier and mucus secretion[49]. During the ALI, the TEER value was measured after adding the culture medium to the insert and equilibrating in the culture incubator for 30 min. When the measurement was finished, the culture medium was removed to maintain ALI. The formal experiment was allowed to be conducted when the TEER values were stable. Cy5-NC@L, Cy5-NC@L-Lf, and Cy5-NC@L-Lf with NAC (Cy5-NC@L-Lf + N), all at the same concentration of Cy5-NC, were added to the insert in a volume of 0.5 mL, with 1 mL of fresh medium in the lower chamber. At the predetermined time points of 2, 6, and 12 h, 0.2 mL of the medium in the lower chamber was collected and the same amount of fresh medium was supplemented. The standard curve for the apparent fluorescence intensity of the LNPs *in vitro* was constructed, meanwhile, the apparent permeability coefficient (P_{app}) was quantified, which was calculated as Eq. (2):

$$P_{\mathrm{app}} = \frac{\mathrm{d}Q}{\mathrm{d}t} \times \frac{1}{C_{\mathrm{o}} \cdot A} \tag{2}$$

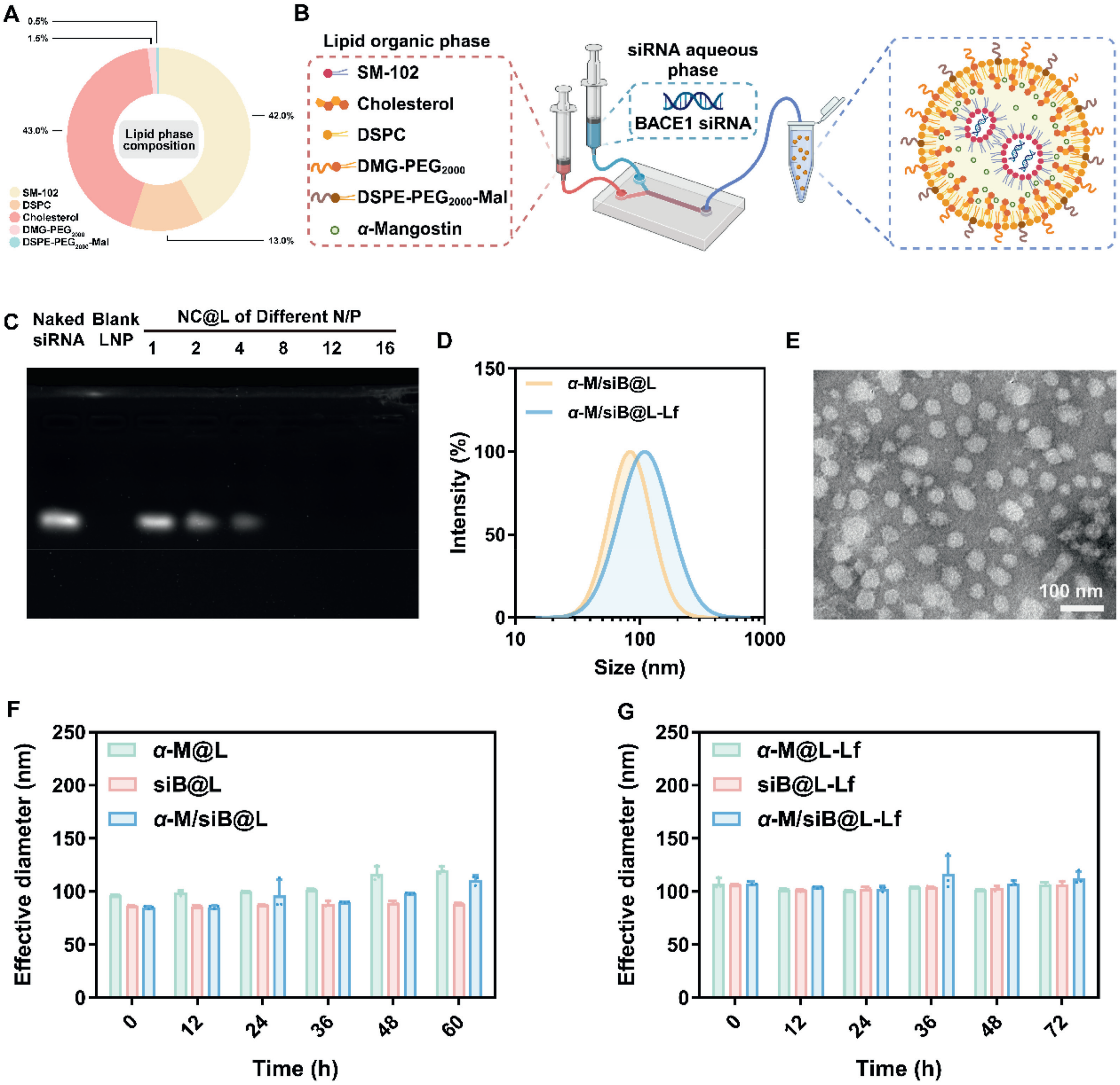

Figure 1 Preparation and characterization of LNPs. (A) The molar percentage of the lipid phase composition. (B) A schematic illustration of the construction of α-M/siB@L *via* microfluidic-chip device. (C) Agarose gel electrophoresis of naked NC, blank LNP, and NC@L at different N/P ratios. (D) Hydration particle of α-M/siB@L and α-M/siB@L-Lf. (E) TEM image of α-M/siB@L-Lf stained by uranyl acetate solution. Scale bar represents 100 nm. Changes of the particle size of (F) LNP preparations and (G) Lf-decorated LNP preparations in PBS at 4 °C (n = 3 per group). Data are presented as mean ± SD.

dQ/dt was the rate of change of the amount of Cy5-NC (Q) over time (t), C_0 was the initial concentration of Cy5-NC, and A was the surface area of the membrane in the insert.

Additionally, the upper chamber monolayer membranes were harvested at different time points and observed *via* CLSM (Leica).

2.12. *Brain targeting study*

C57BL/6 mice were randomly divided into three groups (5 mice per group) and intranasally administered with 20 μL of Cy5-NC@L, Cy5-NC@L-Lf, and Cy5-NC@L-Lf + N, each at the same concentration of Cy5-NC. Mice were executed at 0.25 and 1 h post administration to separate their brains and main organs. The Lumina III Imaging System (PerkinElmer, Waltham, USA) was employed for *ex vivo* fluorescence imaging. Then, the brain tissue was fixed in 4% paraformaldehyde solution for 24 h, dehydrated with 15% and 30% sucrose solution for 48 h, and sectioned at 10 μm by freezing microtome (Leica CM1950, Germany). Ultimately, brain tissue frozen sections were stained with DAPI (2 μg/mL) and observed *via* CLSM (Leica).

2.13. *Treatment for APP/PS1 transgenic mice*

10-Month-old APP/PS1 mice were randomly divided into 5 groups (6 mice per group). C57BL/6 mice were used as control (WT). α-M and siB loaded-LNP (α-M/siB@L), Lf-modified siB loaded-LNP (siB@L-Lf), α-M/siB@L-Lf, and α-M/siB@L-Lf + N were administered intranasally (0.5 mg/kg α-M, 0.5 mg/kg siB, every 2 days for 7 times) to different groups, while PBS (pH 7.2) were given the same way to APP/PS1 mice in AD group as control. Body weight was recorded every 2 days. During the administration, gas anesthesia was administered concurrently. After completion of treatment, behavioral tests were performed.

2.14. *Behavioral test*

Morris water maze (MWM), Y-maze, and nest-building test were adopted to comprehensively evaluate the cognitive function and behavioral status of mice. The experimental protocols followed the approach described in previous studies[50,51]. In addition, the criteria for nest scoring were modified slightly: (0) the paper was not torn, and had no obvious nest site; (1) the paper was torn slightly with no obvious nest site; (2) the paper was torn partially, but the nest site was identifiable; (3) partially torn paper with identifiable nest site; and (4) most of the paper towels were bitten with identifiable nest site.

2.15. *Mechanism explorations in vivo*

After the behavioral tests, blood samples were collected from the mice, then all of the mice were sacrificed to obtain brain tissue. Whole blood and serum samples were sent for complete blood count and blood biochemical analysis, respectively. At the same time, some brains, nasal cavities, and main organs were harvested

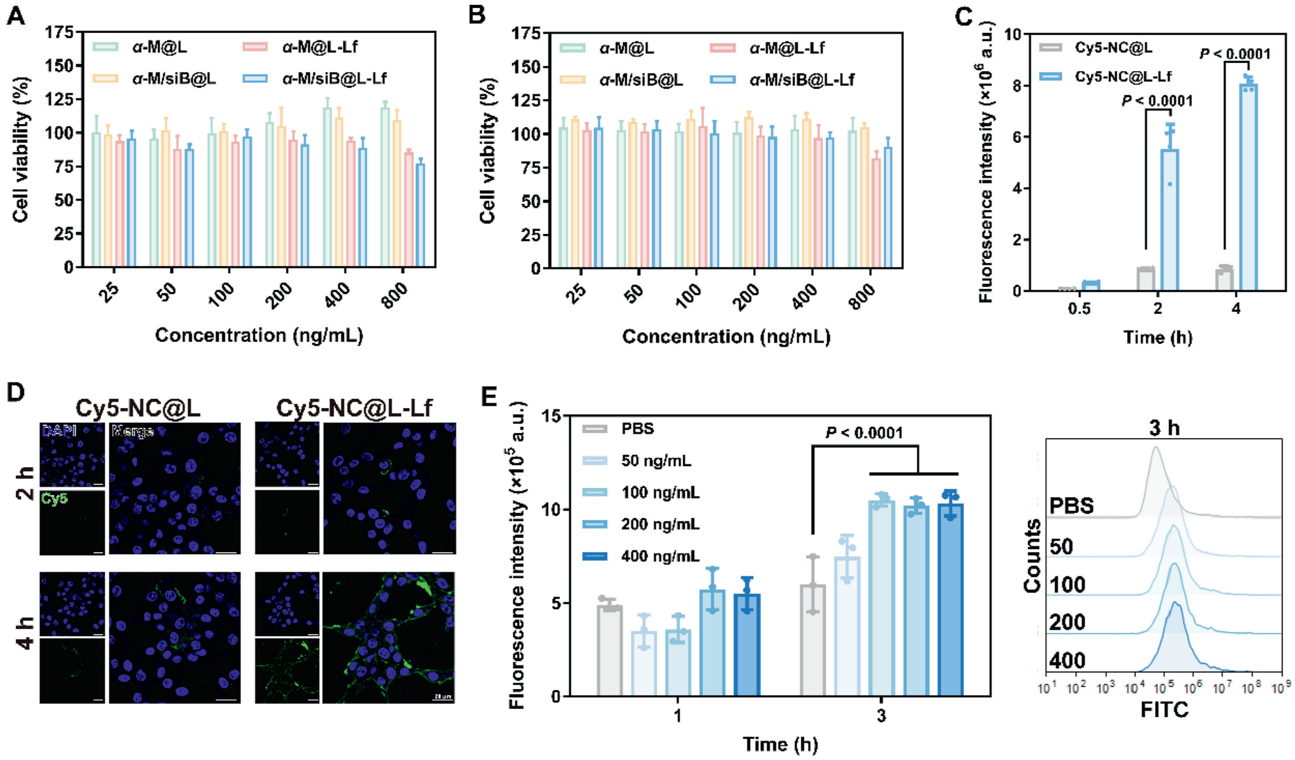

Figure 2 Cytotoxicity, cellular uptake, and the enhanced Aβ internalization *in vitro*. (A) Cell viability of BV-2 cells and (B) PC-12 cells after incubation with LNPs at different α-M concentrations for 24 h measured by MTT assay ($n = 6$). (C) Flow cytometry analysis of cellular uptake of Cy5-NC@L and Cy5-NC@L-Lf at different time points by PC-12 cells ($n = 4$). (D) Fluorescent images of cellular uptake of Cy5-NC@L and Cy5-NC@L-Lf at different time points by PC-12 cells. LNPs were labeled with Cy5 (green). DAPI (blue). Scale bar represents 20 μm. (E) Flow cytometry analysis and quantitative analysis of the uptake of FITC-Aβ at different time points by BV-2 cells ($n = 3$). Data are presented as mean ± SD.

for hematoxylin and eosin (H&E) or Nissl staining to evaluate the cumulative toxicity and neuroprotective effects of the LNPs. Immunohistochemical staining of Aβ, as well as immunofluorescence staining of ROS, GFAP, IBA-1, and NeuN, were performed on brain slices of different groups. Brain RNA and proteins were extracted for qPCR, western blotting, and ELISA.

2.16. *Statistical analysis*

All data were presented as mean ± standard deviation (SD). Statistical analysis was carried out using GraphPad Prism software (version 7.04). One-way analysis of variance (ANOVA) with Tukey's test and two-way ANOVA with Sidak's test were used for the statistical comparison between groups with one independent variable and two independent variable variables, respectively. A significant difference was considered when the *P* value was less than 0.05, and ns represented not significant. Dots overlaid on the bar graphs are the values measured for biological replicates.

3. Results

3.1. *Preparation and characterization of α-M/siB@L-Lf*

Microfluidic-chip device is an extensively exploited LNP fabrication approach to obtain uniform nanoparticles, with high controllability and reproducibility. SM-102, DSPC, cholesterol, DMG-PEG$_{2000}$, and DSPE-PEG$_{2000}$-Mal were dissolved in ethanol according to the formulation (Fig. 1A), which was the lipid organic phase. For α-M-loaded LNP, α-M was also dissolved in ethanol at 1 mg/mL. In addition, the siRNA aqueous phase was prepared by adding the siB into the NaOAc buffer. The two phases were mixed thoroughly to obtain homogeneous LNPs (Fig. 1B).

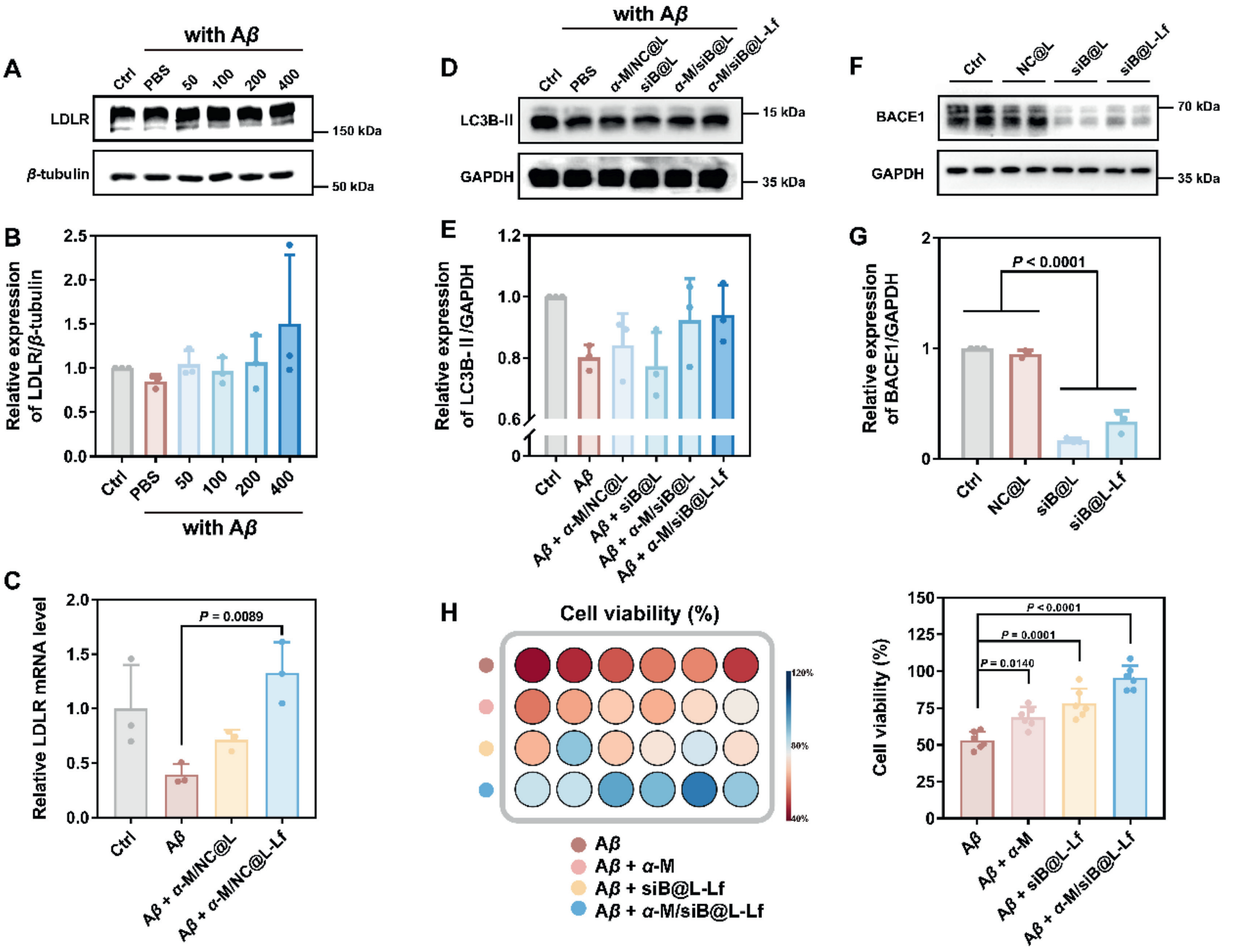

Figure 3 Mechanisms of Aβ elimination and the neuroprotectivity of LNPs *in vitro*. (A) Representative western blotting results of LDLR protein in BV-2 cells after 24 h incubation. (B) The corresponding semiquantitative results of LDLR ($n = 3$). (C) qRT-PCR results of the expression level of LDLR mRNA in BV-2 cells treated with different LNPs and Aβ_{1-42} oligomers ($n = 3$). (D) Representative western blotting results of LC3B-II protein in BV-2 cells treated with different LNPs and Aβ_{1-42} oligomers. (E) The corresponding semiquantitative results of LC3B-II ($n = 3$). (F) Representative western blotting results of BACE1 protein in PC-12 cells after 24 h incubation. (G) The corresponding semiquantitative results of BACE1 ($n = 3$). (H) Heatmap of absorbance values at 490 nm representing cell viability and the quantitative assessment of neuroprotective effects of free α-M and LNPs in PC-12 cells, co-incubated with Aβ_{1-42} oligomers for 36 h ($n = 6$). Data are presented as mean ± SD.

During the mixing, the ionizable headgroup of SM-102 turned to be positively charged and electrostatically bound negatively charged siRNAs in an acidic buffer, allowing stable siRNA encapsulation inside the LNPs and offering protection against enzymatic degradation. Agarose gel electrophoresis indicated that a complete encapsulation of siRNA was achieved when the N/P ratio reached 8 (Fig. 1C). The capsulation efficiency of siRNA was 91.85% *via* RiboGreen assay (Supporting Information Fig. S1). The weight ratio of SM-102 to siRNA was 17.22, which was applied for follow-up experiments. For Lf decoration, the modification ratio of Lf was about 56.17% according to the BCA assay (Supporting Information Fig. S2). Then, the encapsulation

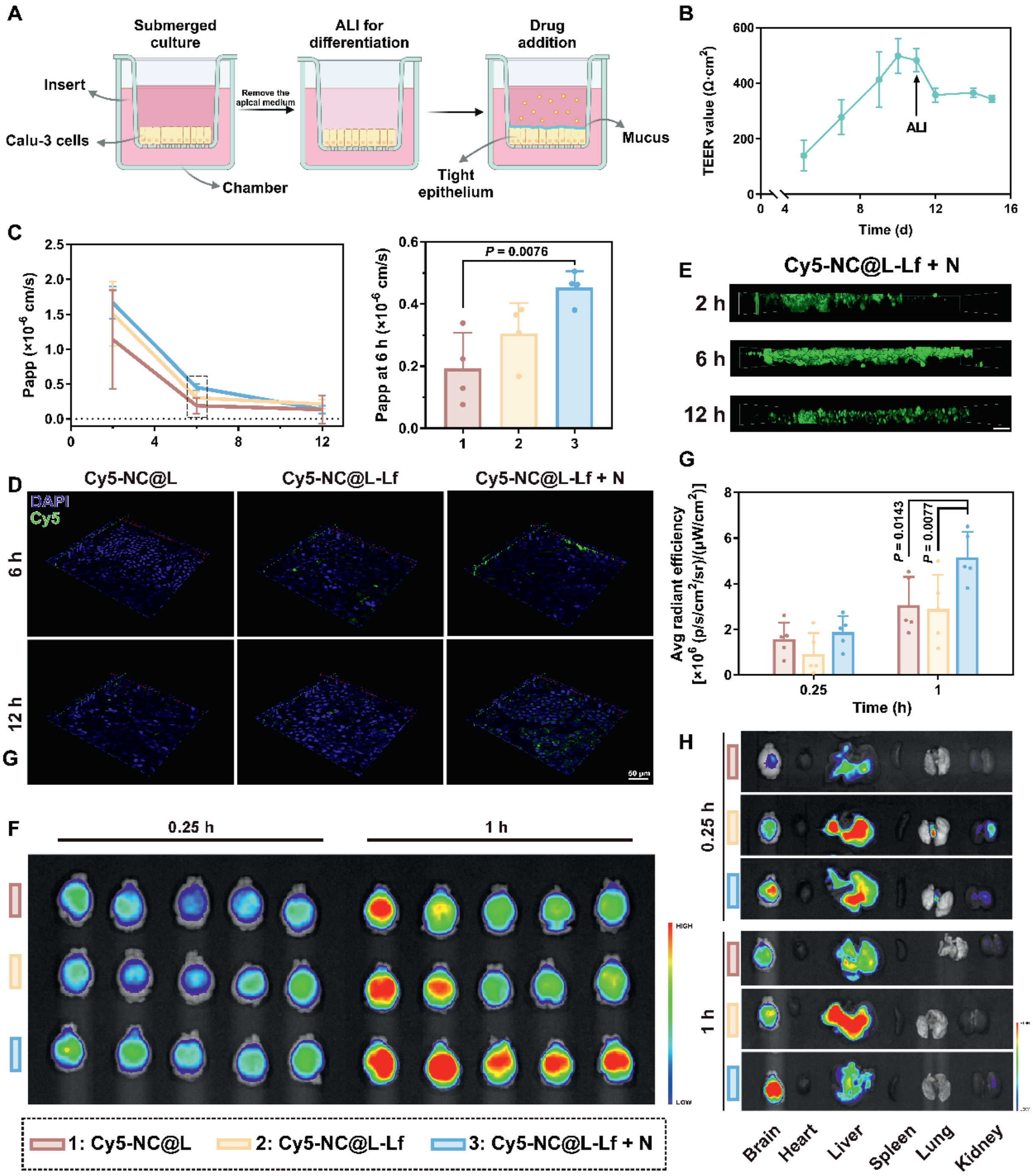

Figure 4 Nose-to-brain targeting efficacy *in vitro* and *in vivo*. (A) The schematic illustration of the nasal Transwell model. Created with BioRender.com. (B) The TEER value of the nasal Transwell model ($n = 16$). (C)The P_{app} curve and the P_{app} of different groups at 6 h ($n = 4$). (D) The CLSM images of LNPs transcytosis by Calu-3 cell model. Scale bar represents 50 μm. (E) The 3D CLSM images of Calu-3 cell monolayers at different time points, displaying the penetration of Cy5-NC@L-Lf + N (green) through the monolayer during the time course. Scale bar represents 25 μm. (F) *Ex vivo* fluorescent imaging and (G) the semi-quantification of brain average radiant efficiency at 1 h post-administration of Cy5-labeled LNPs ($n = 5$). (H) Representative *ex vivo* imaging of major organs and brains. Data are presented as mean ± SD.

efficiency and loading capacity of α-M in α-M/siB@L-Lf were determined to be 35.64% and 8.91%, respectively, demonstrating the successful incorporation (Supporting Information Fig. S3). The hydrodynamic diameter determined *via* dynamic light scattering (DLS) of α-M/siB@L and α-M/siB@L-Lf was 84.97 ± 1.44 nm and 107.89 ± 1.34 nm, respectively (Fig. 1D). The surface charge of α-M/siB@L-Lf was −10.62 ± 5.48 mV. The transmission electron microscope (TEM) image revealed the uniform spherical shape of α-M/siB@L-Lf, and the diameter was consistent with the DLS results (39.97 ± 3.57 nm) (Fig. 1E). Moreover, differed from plain spherical morphology, the spheres of the α-M/siB@L-Lf were slightly antenna-like, which might be attributed to the successful conjugation of Lf. The LNPs, especially the Lf-decorated ones, demonstrated excellent storage stability, with no significant changes in particle size observed over 48 h (Fig. 1F and G).

3.2. Amelioration of AD pathology via Aβ scavenging and BACE1 silencing in vitro

According to the thiazolyl blue (MTT) assay, BV-2 cells were more sensitive to the ascending concentration of α-M, which exhibited mild death when the concentration of α-M reached 800 ng/mL (Fig. 2A), while PC-12 showed better tolerance (Fig. 2B). At the same time, the stronger cytotoxicity engendered by Lf-decorated LNPs could be attributed to the higher cellular uptake mediated by Lf. Calu-3 cells are generally utilized to simulate olfactory epithelium transport *in vitro*, which were adopted along with PC-12 cells to verify the reinforced receptor-mediated endocytosis endowed by Lf[43,44,46]. The flow cytometry analysis displayed that, the cellular uptake of Cy5-NC@L-Lf was 9.36- and 4.71-fold higher than Cy5-NC@L for PC-12 cells and Calu-3 cells at 4 h, respectively (Fig. 2C, Supporting Information

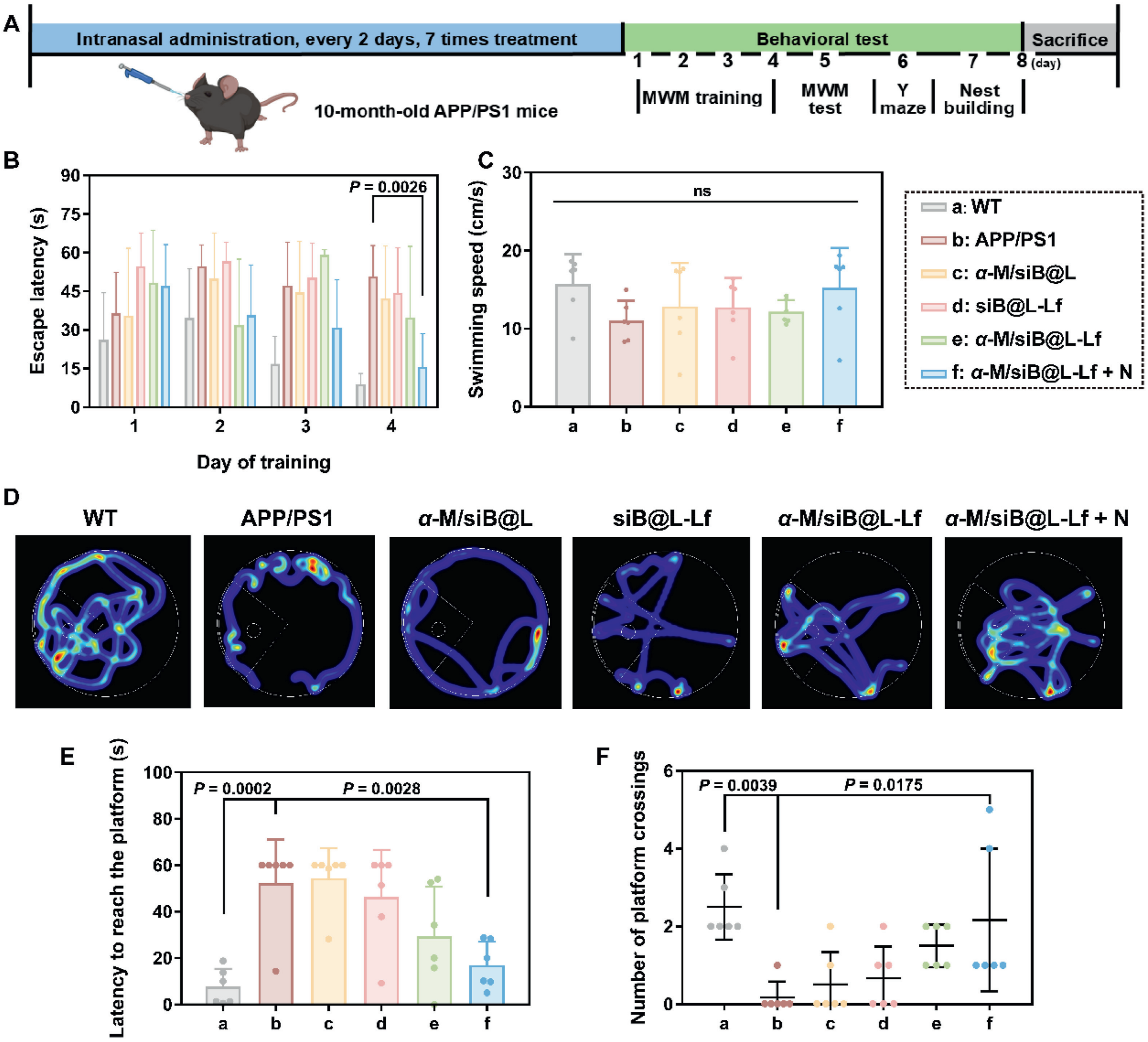

Figure 5 MWM evaluation of LNPs treatment in 10-month-old APP/PS1 transgenic mice. (A) The schematic diagram of the experimental timeline. APP/PS1 transgenic mice received PBS, α-M/siB@L, siB@L-Lf, α-M/siB@L-Lf, and α-M/siB@L-Lf + N treatment, respectively. After every 2 days for 7 cycles, the mice were subjected to MWM, Y-maze, and nest-building test for behavioral evaluation, then the mice were sacrificed and the samples were collected for further assessments. (B) Escape latency during the 4 days of training. (C) The swimming speed of different groups in the test. (D)Representative heatmaps of the swimming path of mice at the test. (E) Latency to reach the platform area and (F) number of platform site crossings at the test. Data are presented as mean ± SD, $n = 6$. ns, not significant.

Fig. S4). The internalization of Cy5-NC@L and Cy5-NC@L-Lf by these cell lines was also observed qualitatively *via* CLSM (Fig. 2D, Supporting Information Fig. S5). The fluorescence of Cy5-NC@L-Lf was more robust than that of Cy5-NC@L at each time point. The results above collectively served as evidence that a conspicuous cellular uptake enhancement was brought in by Lf.

As intracerebral Aβ scavengers, BV-2 cells eliminate Aβ plaques and convert the brain environment from pathological and inflammatory to healthy. Upon the modulation of α-M/NC@L-Lf at different α-M concentrations for 24 h, a significantly augmented uptake of FITC-Aβ was observed *via* both the flow cytometer and the CLSM (Fig. 2E, Supporting Information Fig. S6). Compared to the control group, α-M/NC@L-Lf-treated ones exhibited an enhanced Aβ internalization at 100, 200 and 400 ng/mL of α-M after 3 h, all of which were over 1.70-fold. The LDLR downregulation induced by Aβ oligomers was restored in the presence of α-M/NC@L-Lf, according to the result of western blotting analysis (Fig. 3A and B). The result was further verified in LDLR mRNA level *via* qRT-PCR analysis under the treatment of α-M/NC@L and α-M/NC@L-Lf, and the upregulation efficiency compared to Aβ oligomers-treated groups was 81.19% and 237.55%, respectively (Fig. 3C). These findings collaboratively unveiled that, α-M-loaded LNPs could effectively upregulate the LDLR expression on BV-2 cells, thereby rejuvenating the phagocytosis of Aβ. At the same time, due to the reprogramming of BV-2 cells triggered by α-M, the autophagy activity of α-M/siB@L-Lf-treated groups was elevated by 17.40% compared to Aβ oligomers-treated ones, thus contributing to the promoted degradation of phagocytosed Aβ (Fig. 3D and E). The finding underscored the efficacy of α-M-loaded LNPs in promoting Aβ elimination *via* enhanced LDLR expression, Aβ phagocytosis, and autophagic degradation, thereby assisting the homeostasis restoration in the brain environment.

In addition, siB encapsulated in LNPs showed a significant BACE1 downregulation efficiency. According to western blotting analysis, the silencing efficiency of siB-loaded LNP (siB@L) and siB@L-Lf was 83.44% and 66.38%, while the LNP itself without siB was noneffective (Fig. 3F and G). Moreover, the Aβ-induced BACE1 mRNA increase was also retarded with the treatment of siB@L and siB@L-Lf (Supporting Information Fig. S7). These experiments validated the potential of siB-loaded LNPs in the BACE1 expression knockdown, thus ceasing the Aβ production with α-M in a two-pronged manner.

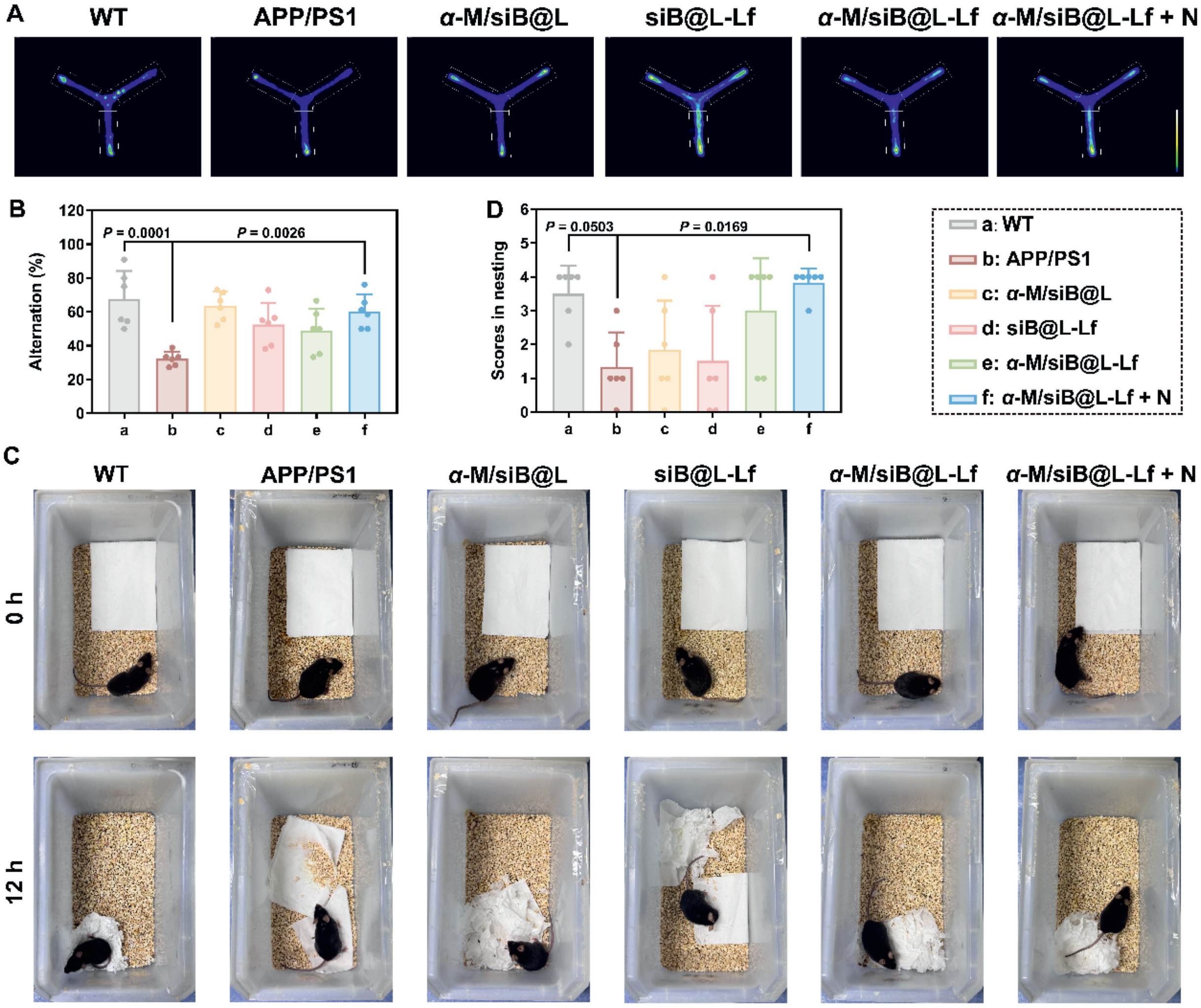

Figure 6 Y-Maze and Nest building evaluation of LNPs treatment in 10-month-old APP/PS1 transgenic mice. (A) Aggregated activity trajectory heatmaps of mice in each group in the Y-maze test. (B) Autonomous alternation rate of each group in the Y-maze test. (C) Representative images of the nest of different groups at 0 and 12 h in the nest building test. (D) The scores in nest building ability of different groups. Data are presented as mean ± SD, $n = 6$.

Ultimately, the neuroprotection of α-M/siB@L-Lf against injury induced by Aβ oligomers was investigated *via* the MTT analysis (Fig. 3H). The survival rate of PC-12 cells decreased to 53.11% after the co-incubation with Aβ oligomers for 36 h. The cell damage was moderately alleviated by the addition of α-M for its polyphenol structure-derived anti-inflammatory effect. Meanwhile, siB@L-Lf also exhibited similar cell viability restoration ability (70.69%), which might be attributed to the siB that deferred the Aβ oligomers-induced pathological deterioration for PC-12 cells themselves. For α-M/siB@L-Lf-treated groups, the cell death ceased utterly, indicating a significant neuroprotective effect (95.59%) introduced by both the α-M and siB.

3.3. *Evaluation of nose-to-brain targeting efficacy both in vitro and in vivo*

To verify the nose-to-brain transmembrane efficiency endowed by Lf conjugation and the addition of permeation enhancer NAC, a nasal epithelial cell model was established (Fig. 4A). Initiated by removing the apical medium and changing the culture condition from submerged to ALI, the differentiation of Calu-3 cells allowed the formation of a functional tight epithelium, thus obtaining an *in vitro* nasal model with tight epithelial barrier and mucus secretion. The TEER values were monitored regularly (Fig. 4B), and the formal experiment was conducted when the TEER value reached a stable level at about 350 $\Omega \cdot cm^2$ after ALI. The medium in the lower chamber and the upper cell membrane were collected after co-incubation for 2, 6, and 12 h, respectively. The P_{app} of Cy5-NC@L-Lf + N groups was 1.66×10^{-6} cm/s at 2 h, manifesting the highest transport rate among the three groups (Fig. 4C). At 6 h, the P_{app} of Cy5-NC@L-Lf + N groups was 1.69- and 1.22-fold compared to Cy5-NC@L and Cy5-NC@L-Lf groups. Similarly, the transcytosis and the penetration through the apical monolayer cell membrane were captured *via* CLSM (Fig. 4D and E), indicating an enhanced uptake and transportation during the time course.

To further validate the potential of LNPs to enter the brain through the nose-to-brain route, the transportation was monitored at 0.25 and 1 h after intranasal administration in C57BL/6 mice *via* near-infrared fluorescence imaging. The Cy5 fluorescence intensity of Cy5-NC@L-Lf + N in the brain at 0.25 and 1 h was both detected as the highest among all groups, demonstrating its prominent brain entry efficiency benefited from both the Lf and NAC (Fig. 4F). The semi-quantification of brain fluorescence showed that the brain accumulation of Cy5-NC@L-Lf + N was 1.68- and 1.78-fold stronger than that of Cy5-NC@L-Lf and Cy5-NC@L at 1 h, showcasing the considerable augmentation of brain targeting and accumulation (Fig. 4G). However, in comparison to the *in vitro* experiment outcomes, a negligible difference was observed in brain-targeting efficiency *in vivo* between Cy5-NC@L-Lf and Cy5-NC@L groups, which might have resulted from the inhibitory effects of nasal mucus and ciliary motion in the nasal cavity, thus emphasizing the indispensability of NAC. Furthermore, the preferential accumulation of Cy5-NC@L-Lf + N in the brain highlighted its superior brain-targeting

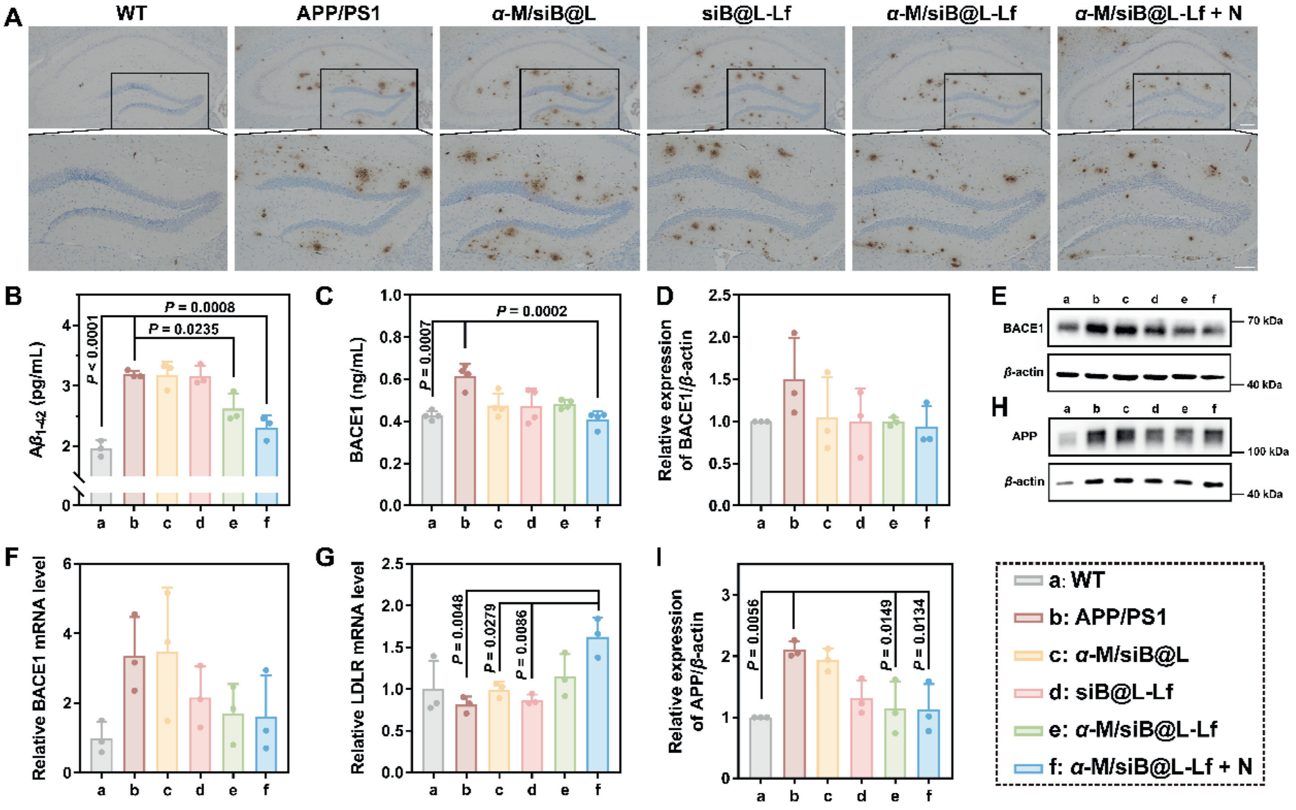

Figure 7 Aβ deposition clearance and the synergistic mechanism. (A) Immunohistochemical staining of Aβ plaques in the hippocampus (HPC) of different groups. Scale bars represent 500 μm for the first line and 200 μm for the second line. (B) Aβ level in the brain determined *via* ELISA ($n = 3$). (C) BACE1 level in the brain determined *via* ELISA ($n = 4$). (D) Semiquantitative results and (E) representative western blotting results of BACE1 in the brain ($n = 3$). (F) qRT-PCR results of the expression of BACE1 mRNA and (G) LDLR mRNA in the brain ($n = 3$). (H) Representative western blotting results of APP protein in the brain and (I) the corresponding semiquantitative results ($n = 3$). Data are presented as mean ± SD.

capability and demonstrated the potential of nose-to-brain LNP delivery (Fig. 4H). Whereafter, the brain tissue at 1 h after administration was frozen-sliced to further confirm the accumulation of LNPs *via* CLSM (Supporting Information Fig. S8). Likewise, the fluorescence intensity of Cy5-NC@L-Lf + N was stronger than that of the other two groups, which was concordant with previous results of the *ex vivo* imaging. The above experiments collaboratively disclosed the prospect that the Lf modification and the addition of NAC are conducive to transport efficiency *via* the nose-to-brain route, which prominently tackled the traditional brain targeting hurdle and refreshed AD therapy.

3.4. *Rescue of cognitive and learning deficits in transgenic mice*

A series of different LNP preparations were applied every two days to 10-month-old APP/PS1 transgenic mice to assess the therapeutic effects on AD (Fig. 5A). APP/PS1 mice were grouped randomly and received intranasal administration with different LNPs and PBS (as a control). WT mice were employed to confirm the AD-relevant deficits in transgenic mice at baseline. On accomplishing the last administration, various behavioral experiments were performed to comprehensively evaluate the cognitive function and behavioral state of mice. During the MWM training, the escape latency of α-M/siB@L-Lf + N group was significantly shortened, exhibiting a great spatial memory and reaching a level similar to that of WT group, while PBS-treated APP/PS1 mice remained unintentional swimming (Fig. 5B). In the test, the mice exhibited similar swimming speed (Fig. 5C), and the swimming trajectories for searching the platform were similar to the results of the training (Fig. 5D, Supporting Information Fig. S9). The mice in the α-M/siB@L-Lf + N group manifested an evident preference for the platform area not only in the time of seeking (Fig. 5E) but also in the crossing frequency (Fig. 5F), which demonstrated the effectiveness of α-M/siB@L-Lf + N treatment in rescuing spatial learning and memory deficits. α-M/siB@L-Lf group also showed moderate improvement, whereas the therapeutic outcome might be constrained by the obstacle in the intranasal mucus penetration. Similarly, the Y-maze test was conducted to analyze the exploratory behavior and short-term memory in a novel environment *via* the activity heatmap and the alternation (Fig. 6A and B). Compared with PBS-treated APP/PS1 mice, all the LNP preparation-treated mice were more active, and the spontaneous alternations of which were remarkably higher and close to the level of WT mice. In the nest building test (Fig. 6C and D), α-M/siB@L-Lf + N-treated mice attained a similar score to the WT mice, further confirming the restoration of impaired innate behavioral execution as well as

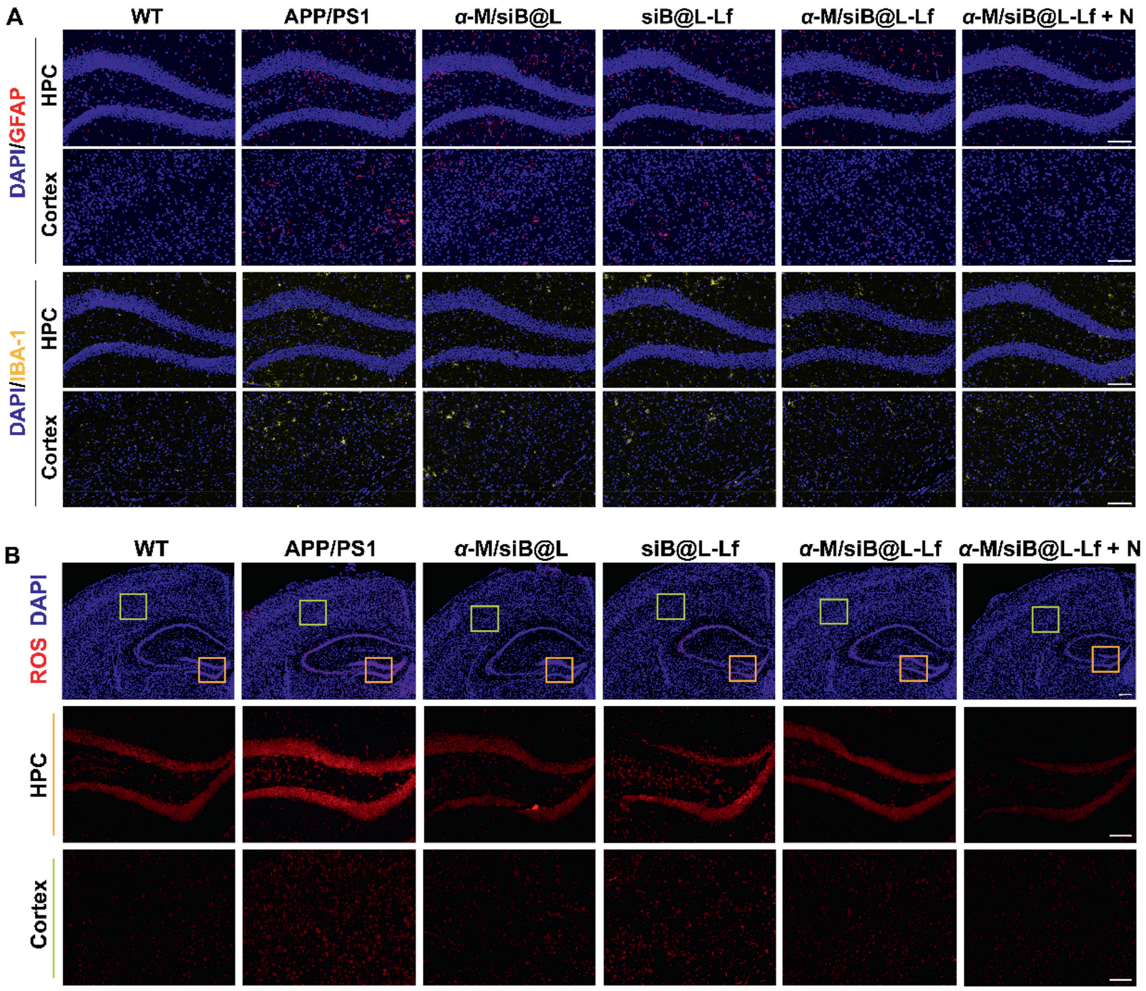

Figure 8 Reduced activation of glial cells and ROS scavenging. (A) Fluorescent images of GFAP and IBA-1 expression analysis of mice brain slices. Scale bar represents 100 μm. (B) Fluorescent images for the detection of ROS level in mice brain slices. Scale bar represent 500 μm for the first line and 100 μm for the others.

cognitive dysfunction in APP/PS1 mice. The above results congruously illustrated that α-M/siB@L-Lf administered along with NAC could attenuate cognitive and learning deficits in APP/PS1 mice, while other LNP-treated groups yielded less satisfactory therapeutic effect due to onefold treatment or lower delivery efficiency, thereby revealing the indispensability of combination therapy for AD and the addition of NAC for nose-to-brain delivery.

3.5. Mutifaceted anti-AD mechanism analysis and biosafety assessment

Aβ deposition and activation of glial cells are leading perpetrators of prolonged neuroinflammation, contributing to overwhelming oxidative stress and prominent neuronal apoptosis. First, the Aβ levels in the brain were determined *via* immunohistochemical staining (Fig. 7A) and ELISA (Fig. 7B). Compared with PBS-treated APP/PS1 mice, the Aβ levels of α-M/siB@L-Lf and α-M/siB@L-Lf + N-treated mice were significantly dwindled. Next, the mechanisms of the Aβ scavenging were explored. ELISA, qRT-PCR, and western blotting analysis showed a general decline of BACE1 expression almost in all LNPs-treated groups (Fig. 7C—F). However, although BACE1 levels were downregulated in α-M/siB@L and siB@L-Lf groups, no thorough improvement was observed in these two groups during previous behavioral experiments, indicating the inadequacy of siRNA monotherapy and the importance of combining α-M and BACE1 siRNA for two-pronged Aβ elimination therapy. Therefore, in addition to BACE1 inhibition to impede Aβ generation, the α-M-triggered upregulation of LDLR

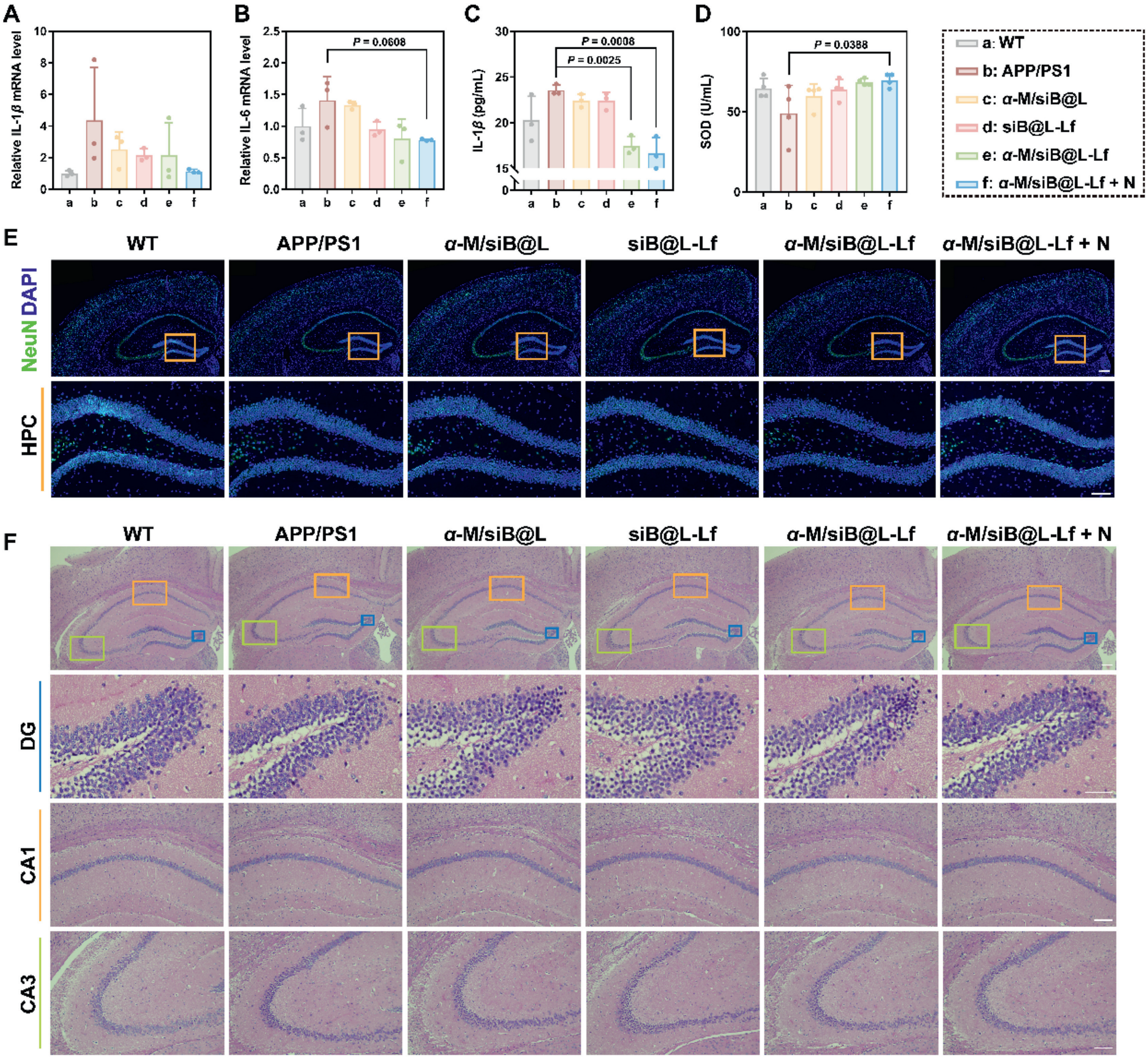

Figure 9 Anti-inflammatory effect and neuroprotection. The levels of pro-inflammatory cytokines (A) IL-1β and (B) IL-6 in the brain after treatment were examined *via* qRT-PCR analysis ($n = 3$). (C) The IL-1β level in the brain after treatments *via* ELISA ($n = 3$). (D) The SOD level in serum after treatment ($n = 4$). (E) Fluorescent images of NeuN in the brain. Scale bar represents 200 μm for the first line and 100 μm for the second line. (F) H&E staining images of brains after treatment. Scale bar represents 500 μm for the first line, 50 μm for the second line, and 100 μm for the last two lines. All Data are presented as mean ± SD.

for enhanced Aβ uptake in the α-M/siB@L-Lf + N-treated group was a significant contributor to scavenge existing Aβ plaques, as verified *via* qRT-PCR analysis (Fig. 7G). Additionally, benefiting from the improved brain environment, the expression of APP, a biomarker representing the pathological progression and severity of AD, was downregulated (Fig. 7H and I). Then, IBA-1 and GFAP were employed to label activated microglia and astrocytes, which were detrimental to the restoration of brain[52-54] (Fig. 8A). The aberrant proliferation and exorbitant activation of these glial cells were devastating the brains of APP/PS1 mice, whereas the α-M/siB@L-Lf and α-M/siB@L-Lf + N treatments were capable of appeasing the excess activation and boosting the normalization of the brain microenvironment.

The alleviation of Aβ burden as well as the reduced activation of glial cells could efficiently lessen the ROS damage and refine the brain environment. With DHE probe staining indicating the ROS level (Fig. 8B), a powerful ROS scavenging could be spotted in the α-M/siB@L-Lf + N-treated group, which was achieved *via* both the combination therapy and the effective drug delivery. To quantify the level of inflammatory-related cytokines, qRT-PCR analysis and ELISA were performed. IL-1β and IL-6 are crucial pro-inflammatory cytokines, which were diminished after the treatment of α-M/siB@L-Lf and α-M/siB@L-Lf + N (Fig. 9A−C). The elevated levels of superoxide dismutase (SOD) (Fig. 9D) in serum further demonstrated a significant reduction in oxidative stress. Additionally, neuronal marker NeuN was applied to detect the neuron (Fig. 9E). An apparent apoptosis could be observed in the brain of APP/PS1 mice, while the α-M/siB@L-Lf + N treatment rescued the neuron damage and revitalized the neuron density. Then, the results obtained *via* H&E staining (Fig. 9F) and Nissl staining (Supporting Information Fig. S10) reached a similar conclusion, that the distinct nuclear shrinkage and damages were ameliorated, which supported the rehabilitation of memory and learning ability.

Eventually, the systemic toxicity of these LNP formulations was evaluated. First, during the process of intranasal administration, the body weight among the groups was stable (Supporting Information Fig. S11). Also, no noticeable pathological abnormalities were observed in major organs with H&E staining (Supporting Information Fig. S12), complete blood count analysis, and blood biochemical examinations (Supporting Information Figs. S13 and S14). Moreover, the nasal cavities of each group were observed *via* H&E staining (Supporting Information Fig. S15), with intact structures, bushy cilia, and no pathological changes. Taken together, these results showed the good *in vivo* biocompatibility of these LNPs.

4. Conclusions

In this study, we engineered a sophisticated multifunctional lipid nanoparticle system (α-M/siB@L-Lf) tailored for direct nose-to-brain delivery, offering a comprehensive strategy to combat the multifactorial pathology of AD. First, Lf functionalization of LNP facilitated receptor-mediated transcytosis across the nasal epithelial barrier, enabling direct brain targeting while minimizing systemic circulation exposure. To further improve nasal epithelial penetration and prolong residence time, NAC was incorporated as a mucolytic agent, facilitating efficient traversal of the nasal epithelial barrier and amplifying brain bioavailability.

This nanosystem leveraged the synergistic therapeutic potential of α-M and siB—enhancing Aβ clearance through microglial reprogramming and autophagic activation, while simultaneously suppressing Aβ production *via* precise BACE1 silencing. *In vitro* investigations demonstrated that α-M effectively restored Aβ-induced LDLR suppression, potentiating microglial phagocytosis and autophagic degradation of Aβ, while siB achieved potent BACE1 knockdown to mitigate Aβ synthesis. *In vivo* studies in APP/PS1 transgenic mice exhibited profound cognitive restoration, significant attenuation of Aβ plaque burden, and substantial alleviation of neuroinflammation and oxidative stress. Of note, the synergistic integration of NAC with Lf-modified LNPs markedly enhanced delivery efficiency, resulting in superior therapeutic outcomes.

In summary, this meticulously designed system exemplified a transformative, non-invasive, and biocompatible therapeutic paradigm for AD. By harnessing the combined strengths of targeted LNPs, mucolytic enhancement *via* NAC, and a multi-modal therapeutic mechanism, this platform effectively addressed both upstream and downstream pathological hallmarks of the disease. These findings not only underscored its remarkable therapeutic potential but also established a robust foundation for the clinical translation of nose-to-brain delivery systems in the treatment of neurodegenerative disorders.

Acknowledgments

The authors would like to thank Sichuan Provincial Key Laboratory of Philosophy and Social Sciences for Intelligent Medical Care and Elderly Health Management, Key Laboratory of Target Discovery and Protein Drug Development in Major Diseases at Chengdu Medical College of Sichuan Province, and Radiation Processing Key Laboratory of Sichuan Province. The work was supported by the Research and Development Program of the Science and Technology Department of Sichuan Province (2022JDJQ0050, China) and the Key Laboratory of Target Discovery and Protein Drug Development in Major Diseases at Chengdu Medical College of Sichuan Province 2023 Annual Project (23LHZY04, China).

Author contributions

Conceptualization: Weiwei Zhang, Huile Gao, Yanyan Xu. Methodology and investigation: Yanyan Xu, Xiangtong Ye, Yanfeng Du, Wenqin Yang, Fan Tong, Wei Li, Qianqian Huang, and Yongke Chen. Visualization: Yanyan Xu. Supervision: Weiwei Zhang, Huile Gao and Hanmei Li. Writing - original draft: Yanyan Xu and Huile Gao. Writing − review & editing: Huile Gao, Weiwei Zhang, and Yanyan Xu. All of the authors have read and approved the final manuscript.

Conflicts of interest

The authors affirm that there are no known financial or personal conflicts of interest that could have appeared to influence the work reported in this paper.

Appendix A. Supporting information

Supporting information to this article can be found online at https://doi.org/10.1016/j.apsb.2025.02.035.

References

1. Nichols E, Steinmetz JD, Vollset SE, Fukutaki K, Chalek J, Abd-Allah F, et al. Estimation of the global prevalence of dementia in 2019 and forecasted prevalence in 2050: an analysis for the Global Burden of Disease Study 2019. *Lancet Public Health* 2022;**7**:e105−25.
2. Scheltens P, De Strooper B, Kivipelto M, Holstege H, Chételat G, Teunissen CE, et al. Alzheimer's disease. *Lancet* 2021;**397**:1577−90.
3. 2022 Alzheimer's disease facts and figures. *Alzheimers Dement* 2022; **18**:700−89.
4. Long JM, Holtzman DM. Alzheimer disease: an update on pathobiology and treatment strategies. *Cell* 2019;**179**:312−39.
5. Cummings J, Aisen PS, DuBois B, Frölich L, Jack Jr CR, Jones RW, et al. Drug development in Alzheimer's disease: the path to 2025. *Alzheimers Res Ther* 2016;**8**:39.
6. Karran E, De Strooper B. The amyloid hypothesis in Alzheimer's disease: new insights from new therapeutics. *Nat Rev Drug Discov* 2022;**21**:306−18.
7. Jack Jr CR, Andrews JS, Beach TG, Buracchio T, Dunn B, Graf A, et al. Revised criteria for diagnosis and staging of Alzheimer's disease: Alzheimer's Association Workgroup. *Alzheimers Dement* 2024;**20**: 5143−69.
8. Cheng GW, Xie AH, Yan Z, Zhu XZ, Song YF, Chen TK. Nanomedicines for Alzheimer's disease: therapies based on pathological mechanisms. *Brain-X* 2023;**1**:e27.
9. Mead S, Fox NC. Lecanemab slows Alzheimer's disease: hope and challenges. *Lancet Neurol* 2023;**22**:106−8.
10. Sebastian W, Richard M, Edo R, Shirley N, Carol B. Lecanemab for Alzheimer's disease. *BMJ* 2022;**379**:o3010.
11. Kakkar A, Traverso G, Farokhzad OC, Weissleder R, Langer R. Evolution of macromolecular complexity in drug delivery systems. *Nat Rev Chem* 2017;**1**:63.
12. Burke JF, Kerber KA, Langa KM, Albin RL, Kotagal V. Lecanemab. *Neurology* 2023;**101**:661−5.
13. Avgerinos KI, Ferrucci L, Kapogiannis D. Effects of monoclonal antibodies against amyloid-β on clinical and biomarker outcomes and adverse event risks: a systematic review and meta-analysis of phase III RCTs in Alzheimer's disease. *Ageing Res Rev* 2021;**68**: 101339.
14. Kulkarni JA, Witzigmann D, Thomson SB, Chen S, Leavitt BR, Cullis PR, et al. The current landscape of nucleic acid therapeutics. *Nat Nanotechnol* 2021;**16**:630−43.
15. Adams D, Gonzalez-Duarte A, O'Riordan WD, Yang CC, Ueda M, Kristen AV, et al. Patisiran, an RNAi therapeutic, for hereditary transthyretin amyloidosis. *N Engl J Med* 2018;**379**:11−21.
16. Ledford H. Gene-silencing technology gets first drug approval after 20-year wait. *Nature* 2018;**560**:291−2.
17. Singer O, Marr RA, Rockenstein E, Crews L, Coufal NG, Gage FH, et al. Targeting BACE1 with siRNAs ameliorates Alzheimer disease neuropathology in a transgenic model. *Nat Neurosci* 2005;**8**:1343−9.
18. Wang PZ, Zheng XY, Guo Q, Yang P, Pang XY, Qian K, et al. Systemic delivery of BACE1 siRNA through neuron-targeted nanocomplexes for treatment of Alzheimer's disease. *J Control Release* 2018;**279**:220−33.
19. Yang XT, Yang WQ, Xia X, Lei T, Yang ZH, Jia WF, et al. Intranasal delivery of BACE1 siRNA and rapamycin by dual targets modified nanoparticles for Alzheimer's disease therapy. *Small* 2022;**18**: 2203182.
20. Mei C, Zhan JB, Zhu SZ, Zhang YT, Xiong CE, Wang J, et al. Advances of therapy for Alzheimer's disease: an updated review. *Brain X* 2024;**2**:e68.
21. Korczyn AD, Grinberg LT. Is Alzheimer disease a disease?. *Nat Rev Neurol* 2024;**20**:245−51.
22. Scheltens P, Blennow K, Breteler MMB, de Strooper B, Frisoni GB, Salloway S, et al. Alzheimer's disease. *Lancet* 2016;**388**:505−17.
23. Wang DY, Gu X, Ma XY, Chen J, Zhang QZ, Yu ZH, et al. Nanopolyphenol rejuvenates microglial surveillance of multiple misfolded proteins through metabolic reprogramming. *Acta Pharm Sin B* 2023; **13**:834−51.
24. Yao L, Gu X, Song QX, Wang XL, Huang M, Hu M, et al. Nanoformulated alpha-mangostin ameliorates Alzheimer's disease neuropathology by elevating LDLR expression and accelerating amyloid-beta clearance. *J Control Release* 2016;**226**:1−14.
25. Horejs C. From lipids to lipid nanoparticles to mRNA vaccines. *Nat Rev Mater* 2021;**6**:1075−6.
26. Ferhan AR, Park S, Park H, Tae H, Jackman JA, Cho NJ. Lipid nanoparticle technologies for nucleic acid delivery: a nanoarchitectonics perspective. *Adv Funct Mater* 2022;**32**:2203669.
27. Liu R, Luo C, Pang ZQ, Zhang JM, Ruan SB, Wu MY, et al. Advances of nanoparticles as drug delivery systems for disease diagnosis and treatment. *Chin Chem Lett* 2023;**34**:107518.
28. Wang Q, Jiang QK, Li D, Yang ZM, Gao L, Liu F, et al. Elaborately engineering of lipid nanoparticle for targeting delivery of siRNA and suppressing acute liver injury. *Chin Chem Lett* 2024;**35**:108683.
29. Francia V, Schiffelers RM, Cullis PR, Witzigmann D. The biomolecular corona of lipid nanoparticles for gene therapy. *Bioconjug Chem* 2020;**31**:2046−59.
30. Johnson LT, Zhang D, Zhou K, Lee SM, Liu S, Dilliard SA, et al. Lipid nanoparticle (LNP) chemistry can endow unique *in vivo* RNA delivery fates within the liver that alter therapeutic outcomes in a cancer model. *Mol Pharmaceutics* 2022;**19**:3973−86.
31. Cheng Q, Wei T, Jia YM, Farbiak L, Zhou KJ, Zhang SY, et al. Dendrimer-based lipid nanoparticles deliver therapeutic FAH mRNA to normalize liver function and extend survival in a mouse model of hepatorenal tyrosinemia type I. *Adv Mater* 2018;**30**:1805308.
32. Wei Y, Xia X, Li HM, Gao HL. Influence factors on and potential strategies to amplify receptor-mediated nanodrug delivery across the blood−brain barrier. *Expert Opin Drug Deliv* 2023;**20**:1713−30.
33. Akita T, Kimura R, Akaguma S, Nagai M, Nakao Y, Tsugane M, et al. Usefulness of cell-penetrating peptides and penetration accelerating sequence for nose-to-brain delivery of glucagon-like peptide-2. *J Control Release* 2021;**335**:575−83.
34. Sasaki K, Fukakusa S, Torikai Y, Suzuki C, Sonohata I, Kawahata T, et al. Effective nose-to-brain drug delivery using a combination system targeting the olfactory region in monkeys. *J Control Release* 2023; **359**:384−99.
35. Huang QQ, Chen YK, Zhang WW, Xia X, Li HM, Qin M, et al. Nanotechnology for enhanced nose-to-brain drug delivery in treating neurological diseases. *J Control Release* 2024;**366**:519−34.
36. Zhang SS, Li RQ, Chen Z, Wang XY, Dumont AS, Fan X. Immune cells: potential carriers or agents for drug delivery to the central nervous system. *Mil Med Res* 2024;**11**:19.
37. Goel H, Kalra V, Verma SK, Dubey SK, Tiwary AK. Convolutions in the rendition of nose to brain therapeutics from bench to bedside: feats & fallacies. *J Control Release* 2022;**341**:782−811.
38. Kanazawa T, Akiyama F, Kakizaki S, Takashima Y, Seta Y. Delivery of siRNA to the brain using a combination of nose-to-brain delivery and cell-penetrating peptide-modified nano-micelles. *Biomaterials* 2013;**34**:9220−6.
39. Schaefer ML, Böttger B, Silver WL, Finger TE. Trigeminal collaterals in the nasal epithelium and olfactory bulb: a potential route for direct modulation of olfactory information by trigeminal stimuli. *J Comp Neurol* 2002;**444**:221−6.
40. Hinge NS, Kathuria H, Pandey MM. Engineering of structural and functional properties of nanotherapeutics and nanodiagnostics for intranasal brain targeting in Alzheimer's. *Appl Mater Today* 2022;**26**: 101303.
41. Raghav M, Gupta V, Awasthi R, Singh A, Kulkarni GT. Nose-to-brain drug delivery: challenges and progress towards brain targeting in the treatment of neurological disorders. *J Drug Deliv Sci Technol* 2023; **86**:104756.
42. Han XX, Gong NQ, Xue LL, Billingsley MM, El-Mayta R, Shepherd SJ, et al. Ligand-tethered lipid nanoparticles for targeted RNA delivery to treat liver fibrosis. *Nat Commun* 2023;**14**:75.

43. Elzoghby AO, Abdelmoneem MA, Hassanin IA, Abd Elwakil MM, Elnaggar MA, Mokhtar S, et al. Lactoferrin, a multi-functional glycoprotein: active therapeutic, drug nanocarrier & targeting ligand. *Biomaterials* 2020;**263**:120355.
44. Hu KL, Shi YB, Jiang WM, Han JY, Huang SX, Jiang XG. Lactoferrin conjugated PEG-PLGA nanoparticles for brain delivery: preparation, characterization and efficacy in Parkinson's disease. *Int J Pharm* 2011; **415**:273−83.
45. Liu ZY, Jiang MY, Kang T, Miao DY, Gu GZ, Song QX, et al. Lactoferrin-modified PEG-*co*-PCL nanoparticles for enhanced brain delivery of NAP peptide following intranasal administration. *Biomaterials* 2013;**34**:3870−81.
46. Tang SN, Wang AP, Yan XJ, Chu LX, Yang XC, Song YN, et al. Brain-targeted intranasal delivery of dopamine with borneol and lactoferrin co-modified nanoparticles for treating Parkinson's disease. *Drug Deliv* 2019;**26**:700−7.
47. Jiang RL, Lopez V, Kelleher SL, Lönnerdal B. Apo- and hololactoferrin are both internalized by lactoferrin receptor *via* clathrin-mediated endocytosis but differentially affect ERK-signaling and cell proliferation in caco-2 cells. *J Cell Physiol* 2011;**226**:3022−31.
48. Xia X, Wei Y, Huang QQ, Zhou Y, Wang XR, Shi YL, et al. Counteracting Alzheimer's disease *via* normalizing neurovascular unit with a self-regulated multi-functional nano-modulator. *Acta Pharm Sin B* 2024;**14**:5464−78.
49. Sanchez-Guzman D, Boland S, Brookes O, Mc Cord C, Lai Kuen R, Sirri V, et al. Long-term evolution of the epithelial cell secretome in preclinical 3D models of the human bronchial epithelium. *Sci Rep* 2021;**11**:6621.
50. Huang QQ, Jiang CQ, Xia X, Wang YF, Yan C, Wang XR, et al. Pathological BBB crossing melanin-like nanoparticles as metal-ion chelators and neuroinflammation regulators against Alzheimer's disease. *Research* 2023;**6**:180.
51. Wang XR, Chen SQ, Xia X, Du YF, Wei Y, Yang WQ, et al. lysosome-targeting protein degradation through endocytosis pathway triggered by polyvalent nano-chimera for AD therapy. *Adv Mater* 2024;**37**: 2411061.
52. Yang WQ, Shi YL, Zhang YW, Yang YT, Du YF, Yang ZX, et al. Intranasal carrier-free nanomodulator addresses both symptomatology and etiology of Alzheimer's disease by restoring neuron plasticity and reprogramming lesion microenvironment. *ACS Nano* 2024;**18**: 29779−93.
53. Lei T, Yang ZX, Jiang CQ, Wang XR, Yang WQ, Yang XT, et al. Mannose-integrated nanoparticle hitchhike glucose transporter 1 recycling to overcome various barriers of oral delivery for Alzheimer's disease therapy. *ACS Nano* 2024;**18**:3234−50.
54. Habib N, McCabe C, Medina S, Varshavsky M, Kitsberg D, Dvir-Szternfeld R, et al. Disease-associated astrocytes in Alzheimer's disease and aging. *Nat Neurosci* 2020;**23**:701−6.